PROCEEDINGS OF SCIENCE

Suzaku Wide-band All-sky Monitor – 10 Years history

Masanori Ohno*, **Yasushi Fukazawa, Takafumi Kawano**
Departoment of Physics, Hiroshima University, Japan
E-mail: ohno@astro.hiroshima-u.ac.jp

Kazutaka Yamaoka
Institute for Space-Earth Environmental Research (ISEE), Nagoya University, Japan
Division of Particle and Astrophysical Science, Nagoya University, Japan

Makoto S. Tashiro, Tetsuya Yasuda, Junichi Enomoto, Shunsuke Matsuoka, Tsutomu Nagayoshi, Souhei Nakaya, Sawako Takeda, Yukikatsu Terada, Seiya Yabe
Department of Physics, Saitama University, Japan

Kevin Hurley
Space Sciences Laboratory, University of California, USA

Hans A. Krimm
Universities Space Research Association, USA
National Science Foundation, USA

Amy Y. Lien
Center for Research and Exploration in Space Science and Technology (CRESST) and NASA Goddard Space Flight Center, USA
Department of Physics, University of Maryland, USA

Norisuke Ohmori, Ryuuji Kinoshita, Yusuke Nishioka, Makoto Yamauchi, Hiraku Yoshida
Department of Applied Physics, University of Miyazaki, Japan

Satoshi Sugita
Department of Physics, School of Science, Tokyo Institute of Technology, Japan

Yuji Urata
Institute of Astronomy, National Central University, Taiwan

Yoshitaka Hanabata
Institute of Cosmic-Ray Researh (ICRR), The University of Tokyo, Japan

Wataru Iwakiri
MAXI Team, Global Research Cluster, The Institute of Physics and Chemical Research (RIKEN), Japan

Motohide Kokubun

PoS(FRAPWS2018)046

Department of High Energy Astrophysics, Institute of Space and Astronautical Science (ISAS), Japan

Kazuo Makishima

RIKEN, Japan

Yujin Nakagawa

Advanced Visualization and Computation Research Group, Advanced Earth Information Research Department, Center for Earth Information Science and Technology (CEIST), Japan

Kazuhiro Nakazawa

Department of Physics, The University of Tokyo, Japan
Research Center for the Early Universe, The University of Tokyo, Japan

Takanori Sakamoto

Department of Physics and Mathematics, Aoyama Gakuin University, Japan

We will review the 10 years history of all-sky observations in the hard X-ray to soft gamma-ray energy band by the Suzaku Wide-band All-sky Monitor. The Suzaku-WAM is the shield detector of the Hard X-ray detector onboard Suzaku and the primary purpose is to guard the main detector and the background rejection. In addition, the large effective area of these shield detectors (~ 600 cm^2 at 1 MeV and the large field of view ($> 2\ \pi$ str) enable us to perform all-sky observations in $50 - 5000$ keV. During 10 years operations, the WAM detected more than 1400 GRBs and many other transients such as soft gamma repeaters and solar flares. This detection rate of GRBs is comparable to that of other GRB-specific missions. Thanks to its large effective area, a time-resolved properties of these astronomical transients up to the MeV energy band were investigated with good photon statistics.

Frontier Research in Astrophysics - III (FRAPWS2018)
28 May - 2 June 2018
Mondello (Palermo), Italy

*Speaker.

1. Introduction

The hard X-ray and soft gamma-ray sky are very active in every distance scale, from the our solar system to the cosmological distances. In our solar system, the Sun is flaring in the X-ray to gamma-ray energy band with the thermal and non-thermal bremsstrahlung emission and nuclear emission lines, which are thought be originated by the accelerated electrons in the magnetic reconnection[51]. There are many bright gamma-ray sources inside or outside our galaxy such as black hole binaries, pulsar wind nebula and soft gamma repeaters (SGRs) [2], where the gamma-rays come from energetic electrons inside the relativistic jet or some exotic processes. The gamma-ray bursts is the most energetic explosion in the universe at the cosmological distances and the gamma-ray is thought to be generated at the ultra-relativistic outflow by the thermal[5][20][36] or non-thermal processes (e.g., synchrotron emission in internal shocks[8][9][12][14]. Therefore, monitoring these astronomical sources in hard X-ray and soft gamma-ray energy bands is very important because many non-thermal processes become to be dominant for the emission for such energy band and these emission processes could give important information of the particle acceleration physics, jet production mechanism, origin of high-energy cosmic rays etc. Especially, there are many issues remained to be unknown for gamma-ray bursts (GRBs). The origin of GRBs is still under discussion. GRBs are classified into two categories based on its observed duration, long duration GRBs (long GRBs) and short duration GRBs (short GRBs). Recent progress of the rapid follow-up observations with X-ray telescopes and ground based optical telescopes have been revealed that some long GRBs accompany the energetic supernovae and this gives the thought that the origin of long GRBs is the collapse of the massive stars(e.g., [1][11][16][23]). However, there are no such observational evidence to discuss the origin for short GRBs. Theoretically, it is thought that the origin of short GRBs is the merge of the compact binaries such as neutron-neutron, or neutron-blackhole mergers (e.g., [5][6][28]). Association with the gravitational wave signals from such compact binaries and the gamma-ray signals from short GRBs could be a direct evidence for the origin of short GRBs. In addition to such direct observational evidence, a detail comparison of these two classes is also important to investigate if there several types of origins for GRBs. Another important issue to be solved is the gamma-ray emission mechanism of GRBs. The observed gamma-ray spectrum shows a featureless, broken-power-law shape, which can be explained by both the non-thermal synchrotron radiation and the thermal emission from the photosphere. One of the key analysis to solve this problem is the time-resolved spectroscopy. The evolution of the spectral parameters should depend on the emission mechanism. In order to investigate those objectives, good photon statistics from many GRBs are essential and the detector with large effective area with large field of view can provide such observations. In addition, such observations is also very useful to perform a detailed spectroscopy for other astronomical transients such as solar flares and SGRs. The Suzaku Wide-band All-sky Monitor (Suzaku-WAM) is a very powerful all-sky monitor with very large effective area ($\sim$ 600 cm^2 at 1 MeV), covering very wide energy band from 50 to 5000 keV band. The Suzaku-WAM has been operated 10 years from 2005 to 2015 and observed many astronomical transients including more than 1400 GRBs. The WAM successfully detected MeV photons from many bright GRBs and the SGR flare. In this paper, we will review the highlights of the scientific results obtained by the WAM in the §3 after a brief overview of the WAM detector and its in-orbit operations are shown in the §2. Most of materials in this paper have been taken

from another review paper; Yamaoka et al. (2017). See this paper for more detail and any other topics.

2. Suzaku Wide-band All-sky Monitor

The Hard X-ray Detector[30] onboard Suzaku[29] is a compound-eye phoswitch detector, consists of compound-eye Si-PIN semiconductors and GSO scintillators as the main detector, which are installed in the bottom of well-shaped BGO scintillators to reduce the background as shown in the figure 1. In addition, these phoswitch detectors are surrounded by 20 large(40cm height) and thick(4cm) BGO crystals to guard the main detector from the energetic cosmic ray and the further background rejection by the anti-coincidence technique. Thanks to such detector design to minimize the background, the HXD achieved observations with a very good sensitivity in the hard X-ray band. As seen in the figure 1, the shield detectors can observed the all-sky with large effective area, therefore, we have designed to these shield detectors not only for the shields but also for the all-sky monitor and we call this shield detectors as the Wide-band All-sky Monitor (WAM). Figure 2 shows the comparison of the effective area and the energy coverage of the WAM to the other dedicated GRB missions and it is clearly see that the WAM can cover the wide energy range from 50 to 5000 keV and has very large effective area of $\sim$600 cm^2 even at 1 MeV. The effective area of the WAM above 300 keV is largest among any other all-sky monitors despite that the WAM is not the dedicated GRB mission.

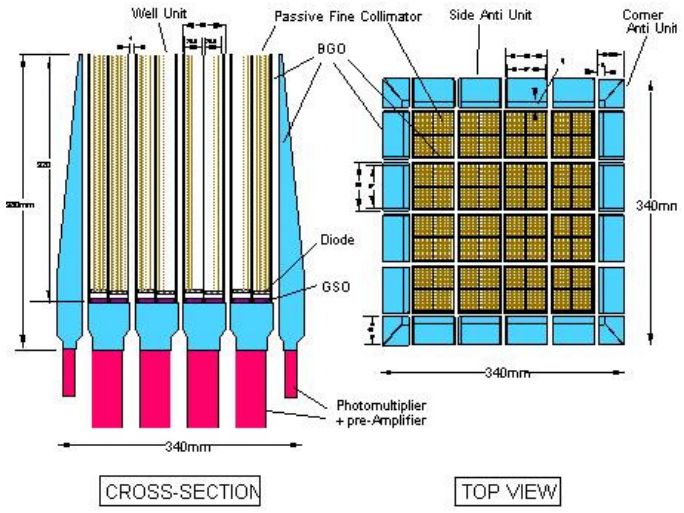

Figure 1: Schematic view of the Suzaku Hard X-ray Detector (HXD): side (left) and top (right) views. The Wide-band All-sky Monitor (WAM) is shown as the cyan part, which surrounds the main detector of the HXD.

2.1 Data types and on-board trigger algorithm

The WAM has two data modes, one is the continuous data (TRN data) which can accumulated the energy spectrum with 55 channel energy bins but coarse time resolution of 1 sec (PH data). The

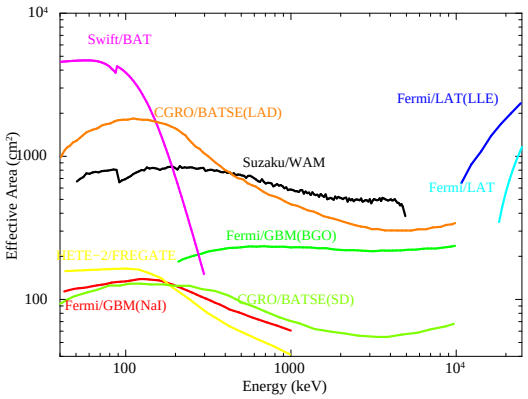

Figure 2: Comparison of the on-axis effective area.

WAM also accumulate finer time history data (TH data) with 15.625 ms (1/64 s) time resolution but only 4 energy channels. This fine time resolution data is always overwritten in the on-board ring buffer on the SRAM, which covers the data length of 64 s, but once the on-board trigger is activated by the following trigger algorithm, the data on the ring buffer will be freezed after it records the data 56 s after the trigger. Then, the data including 8 s of pre-trigger data and 56 s of post-trigger data is stored in the memory. The stored data is transferred to the system data storage during South Atlantic Anomaly (SAA) passage not to suppress the data rate for other main instruments. Please note that the time resolution of the TH data has been changed from 1/32 s to 1/64 s after March 10th 2006. Thus the TH data before this epoch cover the data length of 128 s (16 s of the the pre-trigger and 112 s of the post-trigger). The BST data also contain the PH data, which is equivalent to the TRN data before we set the time resolution of the TH data to be 1/64 s. After that, the time resolution of PH data in the BST data became to be 0.5 s. The summary table of the data format of the WAM can be found in table 1. Figure 3 and 4 show the example of the GRB data obtained by the WAM and it can be clearly seen that the WAM can detect the MeV photons from bright GRBs. The on-board trigger algorithm of the WAM is very simple based on Poissonian fluctuation. The on-board judgment logic calculates statistical fluctuations of the background and judges whether a rate increases is well above the Poissonian fluctuations by following formula,

$$S - \frac{B_g}{\delta bg}\delta t > \sigma\sqrt{\frac{B_g}{\delta bg}\delta t} \tag{2.1}$$

, where S is total counts during a sampling time of δt (1/4 s or 1 s), B_g is background counts, δ bg is the background integration time, which is fixed to be 8 s and σ is the judgment significance level, which is can be selected from 5.7, 8.0, 11.2, and 16.0. After the initial parameter tuning phase, we set the judgment level to be 5.7[24].

2.2 Localization capability

Since the WAM has independent four detectors which are oriented to the different directions,

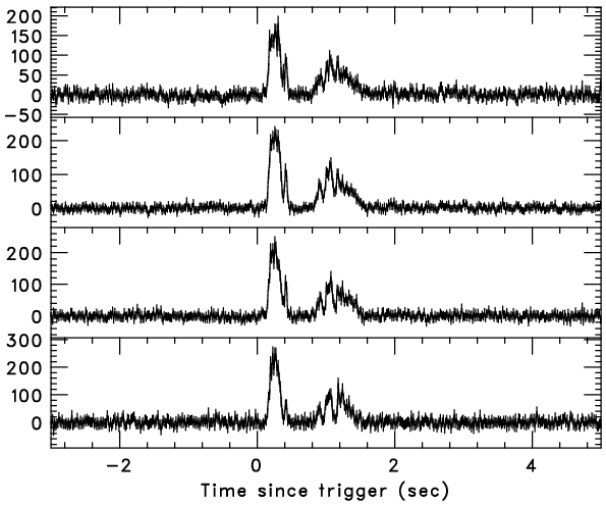

Figure 3: Typical WAM BST data light curve for the bright GRB 060317. Four panels show the four energy channels of the BST data: 50-110, 110-240, 240-520, and 520-5000 keV, respectively from top to bottom[42].

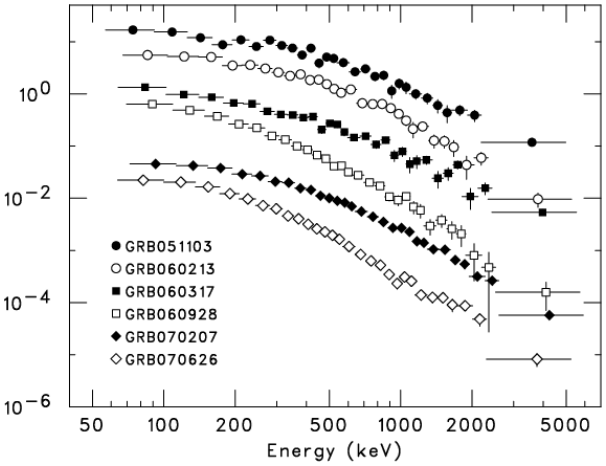

Figure 4: Typical WAM spectra for 6 bright GRBs[42]

the difference of the angular response causes the different observed counts for each four detectors depending on the incoming photon direction. This means that the WAM could have the localization capability of GRBs by comparing such different observed count rate and the expected one based on simulations as was done by the CGRO-BATSE[4] and the Fermi-GBM[55]. We have investigated the capability of the GRB localization by the WAM by using full Monte Carlo simulations which is also used for calculations of the detector responses. Figure 5 shows the calculated expected detection efficiency of four detectors of the WAM as a function of the incoming photon direction for the detector coordinate (θ, ϕ). This figure shows that all WAM detectors except for the WAM-2 (left-bottom) show a relatively simple angular response; the detection efficiency increases for

Table 1: Characteristics of the WAM data (TRN and BST data)[42]

Data Type	Epoch	Energy	Time resolution	Time coverage
BST	2005 Aug 22 - 2006 Mar 20	4ch	1/32 s (TH)	128 s (16 s before and 112 s after the trigger)
		55 ch	1 s (PH)	
	2006 Mar 20-	4ch	1/64 (TH)	64 s (8 s before and 56 s after the trigger)
		0.5 s (PH)		
TRN	2005 Aug 22 -	55ch	1s (PH)	Always transferred to the telemetry every 1 s

the on-axis angle of each detector as a cosine function. The WAM-2 detector shows complicated angular response due to the absorption by the satellite structure since the WAM installed inside the satellite and the absorption by the heavy structure such as cooling dower of the microcalorimater makes such complicated absorption features. Then, we can compare such detection efficiency map and actually observed counts for each detector. Figure 6 shows an example of this procedures for bright GRB 140306A. We can constrain the best-fit position by minimizing the χ^2 for this expected model efficiency and the actually observed counts, however, we found that we can not constrain the GRB position uniquely for almost all cases probably due to lack of a variety of the detector orientation compared with the BATSE and the GBM[56].

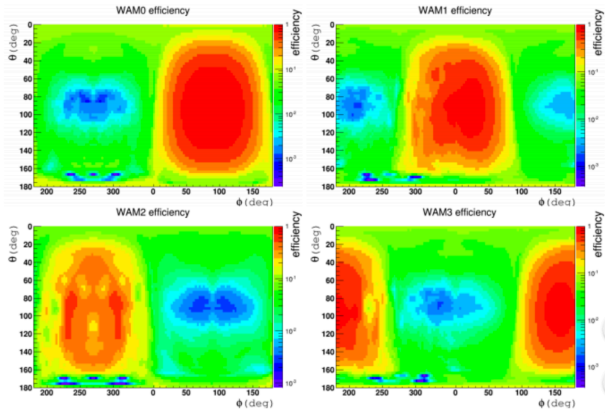

Figure 5: The effective area map of WAM four detectors as a function of the incident GRB position in the detector coordinate. Each panel show the map for each WAM detector (top-left: WAM-0, top-right: WAM-1, bottom-left: WAM-2, and bottom-right: WAM-3, respectively)

2.3 WAM operation history

As described in §2.1, the WAM always accumulate the all-sky data with 1 s time resolution. Figure 7 shows the example of the background light curve obtained by one WAM detector. The background rate per WAM detector is around a few kHz depending on the amount of charged

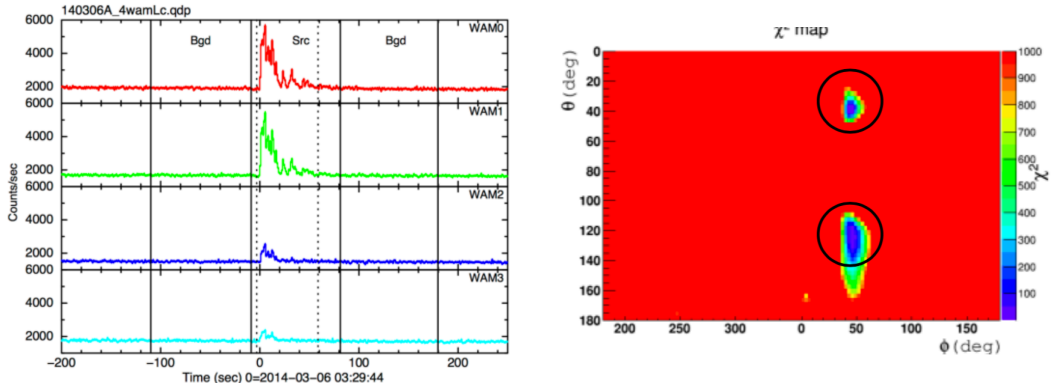

Figure 6: Example of the localization result of the WAM for the bright GRB 140306A. The χ^2 minimization approaches for the observed counts (left) and expected one as a function of the incident angle (fig 5) show a two candidates of the χ^2 minimum, and can not constrain the unique position for this case[56]

particles which is cut by the Earth's magnetic field. Since the inclination of the orbit of Suzaku is 53 degree, Suzaku passes the SAA several times per day. The high-voltage of the photo-multiplier tube (PMTs) of the WAM detector set to be zero to prevent the damage by the trapped charged particles during the SAA passage. This is why there are some gaps in the daily background light curve. After recovery of the high-voltage, the background rate becomes very high due to the activation of the BGO scintillator. There can be seen the drop of the background rate around the end of the figure 7. This is due to the operation dedicated for checking the gain drift of the WAM detector. Each four WAM detector consists of 5 BGO crystals and the signal from four of these 5 units are summed up in the normal operation. We can switch this summed-up mode off and read out the signal from 5 BGO crystals for each four WAM detector unit to check the gain drift of each detector unit. This is because the background rate becomes to be around 1/4 during this gain check operation. Figure 8 left shows an example of the background spectra of 5 BGO crystals obtained by this "unit scan mode". You can clearly see that the peak structure due to the 511 keV annihilation line from activated materials. By monitoring the peak channel of this 511 keV line, we can monitor the gain drift for all of the detector units. Figure 8 right shows an example of the result of this gain drift for one WAM detector. You can see that the detector gain decreases during 10 years operations and it never stop the gradual decreasing, probably because of degradation of PMT condition such as PMT characteristics itself and/or optical coupling between crystals and PMTs but the detail reason is still unknown. We adjusted the high voltage for each PMT to keep the gain of each unit same as seen in the sudden change of this gain history.

2.4 Cross calibration

The detector response of the WAM is calculated by the full Monte Carlo simulation approach including satellite mass model and it is important to reproduce both the gamma-ray energy response for large BGO crystals and also the absorption by detector materials and satellite structures. The ground calibrations have been performed to measure gamma-ray responses such as the energy resolution and complicated light correction efficiency, and the angular response for both the single WAM detector and assembly of the WAM and satellite structures. This ground calibration

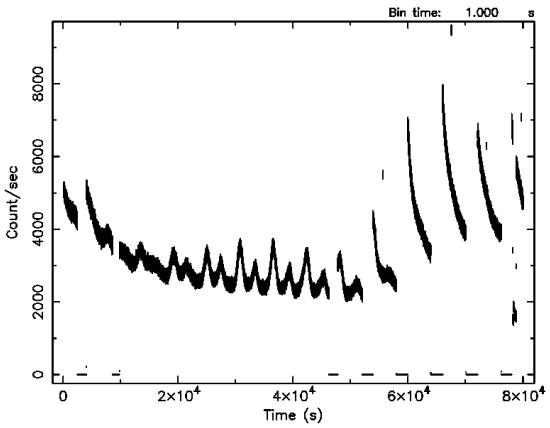

Figure 7: Typical background light curve of one WAM detector for 1-day time interval integrated over all energy band (50-5000 keV).

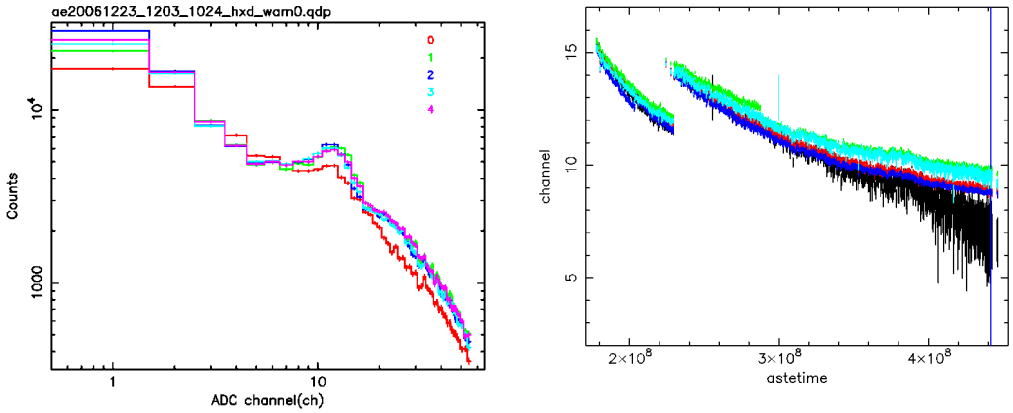

Figure 8: Example of the daily unit-scan spectra of one WAM detector (left). The peak structure around 10 ADC channel corresponds to the 511 keV annihilation line due to the activation of the BGO scintillator. Right panel shows the time history of the ADC channel of this peak structure, so-called the "gain history". The detector gain gradually decreased over all operation periods. Sometimes, the detector gain was adjusted by the high-voltage operation.

procedures successfully provided the detector response which can reproduce measurements within 20-30 % accuracy above 100 keV.[21]. After the launch, the detector response was calibrated utilizing the simultaneously detected astronomical object, mainly GRBs and solar flares. Figure 9 left shows an example of this cross-calibration procedures. In this analysis, we analyzed the GRB data detected by the WAM, the Swift-BAT and the Konus-Wind and check the systematic differences of the obtained spectral parameters for each instrument. Figure 9 right shows the example of the result of this analysis and we found that the uncertainty of the flux and spectral parameters are within 20-30% above 120 keV compared with other detectors for the almost cases[46], which is consistent with that of obtained by the ground calibrations.

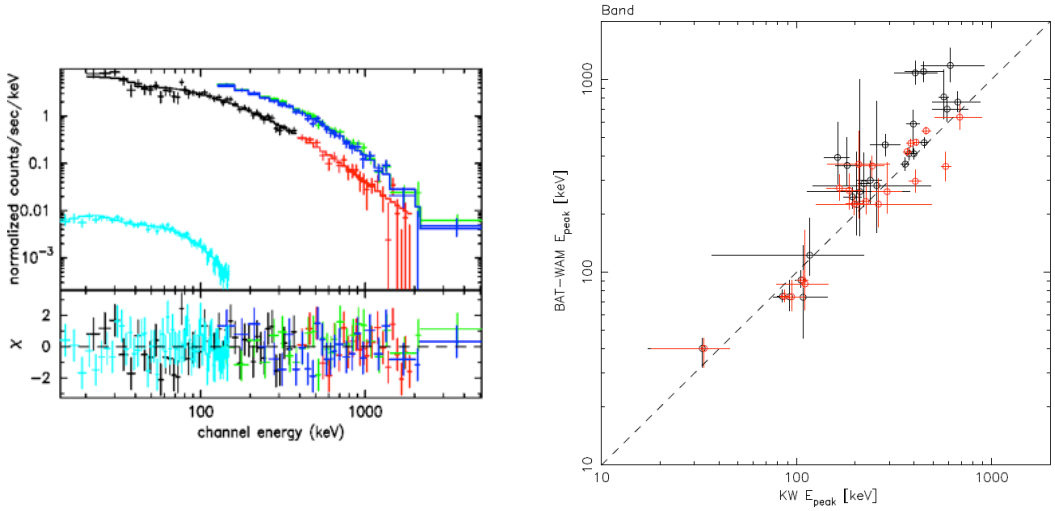

Figure 9: Example of the in-orbit cross calibration spectrum (left) utilizing the GRB spectrum observed by the WAM (green and blue), the Swift/BAT (cyan), and the Konus-Wind (black and red), respectively. These data have been fit by the power-law with an exponential cut-off model or the Band function with the same spectral parameters, but only add the constant factor for each spectra as a free parameter to take into account for the uncertainty of the detector response each other. Right panel show the comparison of the $E_{\rm peak}$ parameter by the analysis using the Konus-Wind and the WAM/BAT joint analysis. Dashed-line represents the case that the two analysis results perfectly agree[46].

3. Highlights of 10 years operations

In this section, we will review the highlights of 10 years operations of the Suzaku-WAM. The WAM has detected more than 1400 GRBs and many other transients. Thanks to its large effective area, not only systematic studies, but also some specific time-resolved spectroscopic analyses have been carried out. The WAM also detected many non-GRB-related transients such as solar flares, SGRs and other bright gamma-ray sources. The wide-energy coverage and a large effective area of the WAM enables us to perform a systematic studies of solar flares and high energy emission from SGRs and gamma-ray sources.

3.1 WAM 10 years trigger statistics

Table 2 shows the summary of the detected astronomical transients and their candidates by the WAM during August 2005 to May 2015. The WAM detected more than 1400 confirmed GRBs, which means the GRBs detected by multiple satellites simultaneously. This means that the GRB detection rate of the WAM was ∼140 GRBs per year, which is comparable to other GRB-dedicated missions. We also detected about 500 possible GRB candidates which includes the GRB events detected only by the WAM. About a half of confirmed and possible GRBs were detected by the on-board trigger, and others were detected by the ground analysis. We have also detected non-GRB related events such as SGRs and solar flares. We have reported both the detection and detailed spectral analysis results to the GCN circular for about 300 circulars, including the localization results by participating to the Inter Planetary Network (IPN). Figure 10 shows the duration distri-

bution of GRBs detected by the WAM. We can see a clear bimodal distribution, which is consistent with BATSE result. This bimodal duration distribution is very important to discuss the subclass of the GRBs, long and short GRBs as described in §1. Ohmori et al (2016) performed a detailed study using 5 year sample and compare to the other instruments to investigated the dependency of the detector sensitivity to this bimodal distribution and reported that the WAM shows a consistent duration distribution to that of other instruments with similar sensitivity. The 10 years statistics shown here is consistent with that of obtained by Ohmori et al. (2016).

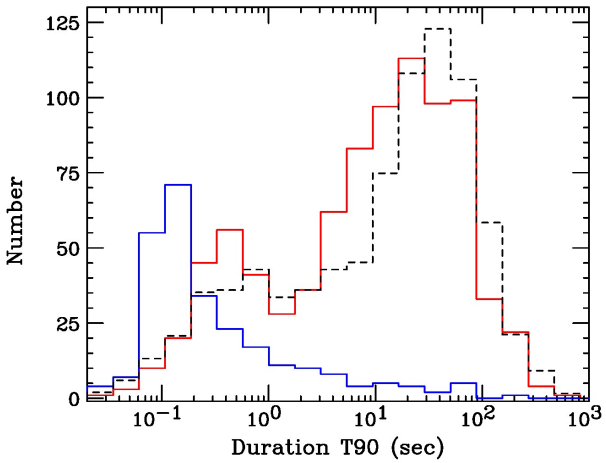

Figure 10: The GRB duration distribution obtained by the WAM 10 years operation data. Red and Blue lines show the confirmed and possible GRBs (see text for detail), respectively. Black dashed-line show the scaled distribution reported by the BATSE[15]

Table 2: WAM trigger statistics (only shows the possible astronomical event)

Event Type	detection number (triggered)
confirmed GRB	1432 (853)
possible GRB	537 (255)
SGR	379 (13)
Solar flare	756 (83)

3.2 GRB spectral parameter distribution

The observed spectrum of GRBs in 10 to 10000 keV energy band are often fit by the phenomenological spectral model which is the smoothly connected broken power-law function so-called Band function [10]. This simple spectral model can be characterized by the photon index in lower energy part, α, the spectral peak energy, $E_{\rm peak}$, and the photon index in upper energy part, β. These spectral parameters should reflect the emission mechanism of GRBs, and therefore it is important to investigate the spectral parameter distribution and compare to other GRB instruments.

3.2.1 single WAM analysis

Figure 11 shows the comparison of distribution of these spectral parameters. Here, we compared the result of the WAM single anaylysis to that of obtained by the Swift-BAT, the Fermi-GBM, and the CGRO-BATSE. We found that the spectral index obtained by the WAM is similar to other instruments, but the distribution of the $E_{\rm peak}$ is somehow different for each other. The distribution shows the peak around 100 keV for the Swift-BAT, 320 keV for the Fermi-GBM, 290 keV for the CGRO-BATSE and 630 keV for the WAM. We consider the difference of the sensitive energy band for each detector could cause such different $E_{\rm peak}$ distribution, therefore, we need the detector or analysis with much wider energy band to obtain an unbiased spectral parameter distribution.

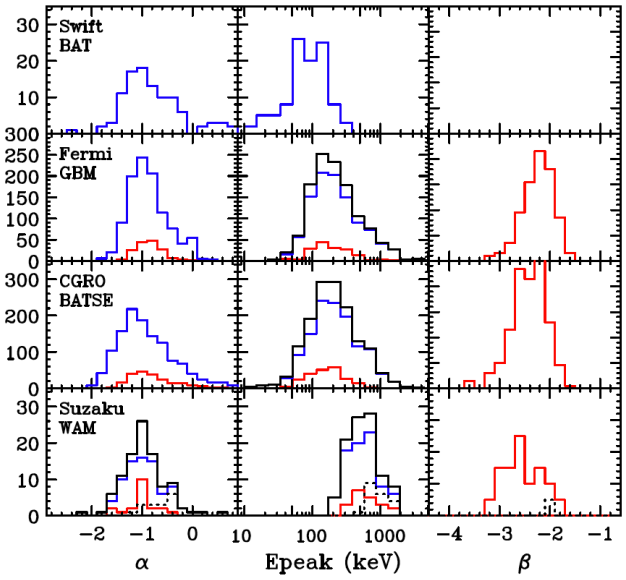

Figure 11: The spectral parameter (the low-energy index α:left, the spectral peak energy $E_{\rm peak}$: middle, and the high-energy index β:right) distribution for the WAM GRBs, compared with Swift/BAT, Fermi-GBM, and CGRO-BATSE fron top to bottom, respectively. The result fit by the single power-law (black), power-law with exponential cut-off (blue) and the Band funtion (red) is shown. Black-dashed line in the WAM data show the short GRBs.

3.2.2 WAM/BAT joint analysis

Then, we carried out the WAM/BAT joint spectral analysis to realize the wider and high sensitive GRB analysis comprehensively from 15-150 keV (Swift/BAT) plus 120 to 5000 keV (WAM). Figure 12 left shows an example of the joint spectra for this analysis and we can clearly see the $E_{\rm peak}$ evolution over wider energy band for each GRB. Figure 12 right is the result of the $E_{\rm peak}$ distribution by this WAM-BAT joint analysis and this distribution becomes to be similar to the distribution obtained by the CGRO-BATSE and the Fermi-GBM. Our analysis should have the highest sensitivity over a wide energy band from 15 to 5000 keV at this moment, and thus we can consider the origin of this parameter distribution from the point of view of the gamma-ray emission mechanism of GRBs. In order to confirm this result, we are now expand this analysis to larger number

samples. The total number of samples will increases from 96 to 245. The result will be discussed in the separated paper.

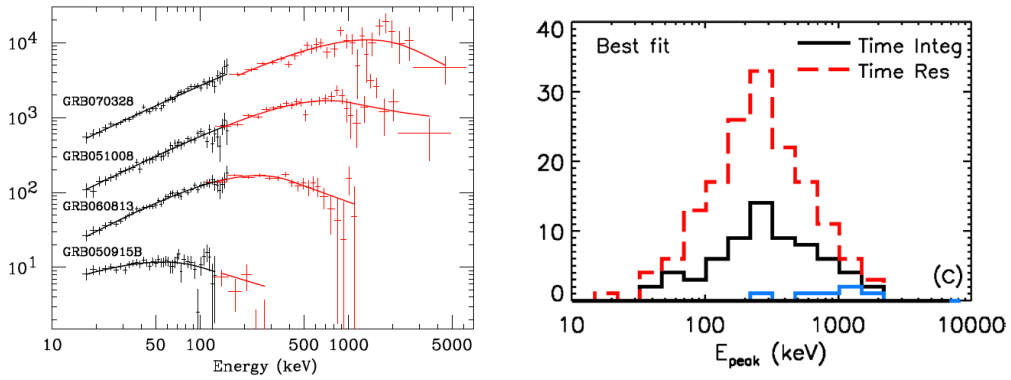

Figure 12: Example spectra of the WAM(red) and BAT(black) joint analysis (left) in the νF_ν plane. Right panel $E_{\rm peak}$ distribution obtained by the WAM-BAT joint spectral analysis. Black-solid and red-dashed line show the result from time-integrated and time-resolved spectral analysis, respectively. Cyan line shows the short GRBs.

3.3 WAM view of the GRB correlations

It is also important to investigate the various spectral parameter correlations to examine the gamma-ray emission mechanism of GRBs. It is well known that the peak energy in the GRB source frame $E_{\rm peak}$ and the isotropic equivalent emission energy $E_{\rm iso}$ for the redshift-known GRBs show a clear correlation with $E_{\rm peak} \propto E_{\rm iso}^{\sim 0.5}$, so-called Amati relation. A similar correlation for the isotropic luminosity for each pulse is also reported by Yonetoku et al. (2004, 2016). The origin of these correlations are still under debate, but this could be an important key to discuss the emission mechanism of GRBs (e.g., $E_{\rm peak} \propto L_{\rm iso}^{0.5}$ is expected by a synchrotron emission model). Since the selection effect is always addressed, the WAM view of these spectral parameter correlations are investigated here.

3.3.1 $E_{\rm peak} - E_{\rm iso}$ correlation

Krimm et al. (2009) analyzed 29 redshift-known GRBs with the BAT-WAM joint analysis method. The redshift of this sample ranges from z=0.089 (GRB 060505) to 6.295 (GRB050904). The result is shown in figure 13 together with previous results. We found that the BAT-WAM long GRB samples also follow the similar $E_{\rm peak} - E_{\rm iso}$ correlation with the parameter of $E_{\rm peak} = (173 \pm 23) E_{\rm iso}^{0.51 \pm 0.05}$, except for the low-luminosity GRB 060505. Krimm et al. (2009) also found that short GRB samples show a different correlation for this parameter plane. This trend is consistent with previous studies. Further discussions on the selection bias for this correlation is found in the original paper Krimm et al. (2009) and they concluded that this result supports a physical origin of the $E_{\rm peak} - E_{\rm iso}$ correlation.

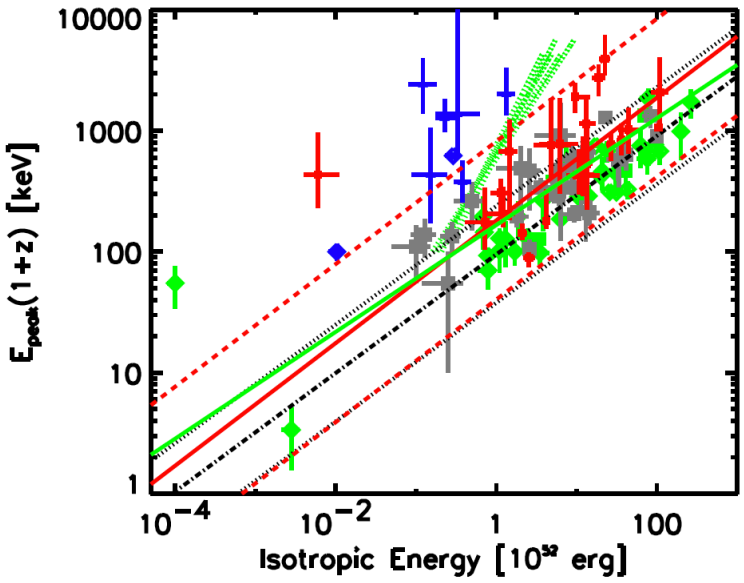

Figure 13: Correlation between $E_{\rm peak}$ and $E_{\rm iso}$ using time-integrated spectra. The red and blue crosses show the WAM data for long and short GRBs, respectively. The previous results are shown by the squares (green squres: Amati (2006), black squares: Cabrera et al. (2007)) and diamonds: Amati (2006). The red-solid and dashed lines show the fit to the BAT-WAM data set and its uncertainty. Black-solid and -dashed lines show the best fit to the previous data. The original figure and caption can be found in the Krimm et al. (2009).

3.3.2 pulse-resolved $E_{\rm peak} - L_{\rm iso}$ correlation

In many cases, the gamma-ray emission from GRBs consist of not a simple pulse but a complicated multiple pulse structure and the spectral parameters are evolved with/within each pulse. Therefore, the spectral parameter correlation is also investigated not only for the integrated pulses but also for the individual pulse-resolved spectra. Golenetskii et al. (1983) suggested the spectral parameter correlation in the $E_{\rm peak} - L_{\rm iso}$ parameter space and following analyses by Lian, Dai, and Wu (2004), Yonetoku et al. (2004), Lu et al. (2012) and Frontera et al. (2012) confirmed that the $E_{\rm peak} - L_{\rm iso}$ follows a similar relation to the $E_{\rm peak} - E_{\rm iso}$ correlation, $E_{\rm peak} \propto L_{\rm iso}^{0.4-0.7}$. We also investigated this $E_{\rm peak} - L_{\rm iso}$ relation by using GRB samples observed by the WAM. Sugita (2010) peformed a detailed analysis of 12 bright, long and multiple-pulse GRBs observed by the WAM, Swift-BAT, and HETE-2. These bursts have been divided into 63 pulses and performed a spectral analysis for all pulses. Figure 14 show the result of the $E_{\rm peak} - L_{\rm iso}$ relation and we found that all of the pulses consistent with $E_{\rm peak} \propto L_{\rm iso}^{\sim 0.5}$ relation as was reported by the previous analysis, but the normalization factor of this relation is somehow different for each burst. The simple synchrotron shock model[18] suggests that if the $E_{\rm peak}$ represents the typical synchrotron energy $\gamma_m m_e c^2$, the relationship between $E_{\rm peak} and L_{\rm iso}$ could be $E_{\rm peak} \propto r^{-1} L_{\rm iso}^{0.5}$, where r is the size of the emitting region, and thus this result support the synchrotron emission scenario with a constant emitting region for one burst, but the emitting region could be different between each burst within one order of magnitude.

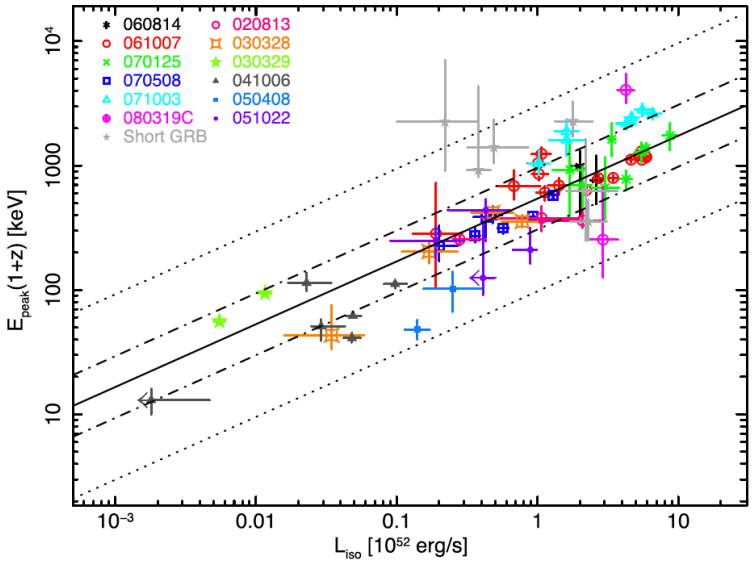

Figure 14: Correlation between $E_{\rm peak}$ and $L_{\rm iso}$ using 63 pulse-resolved spectra from 12 multi-pulsed GRBs. The best fit correlatoin model is shown by the solid-line and 1-σ and 3-σ error regions are shown by the dotted-dashed and dotted lines, respectively[44].

3.3.3 "finer"-resolved $E_{\rm peak} - L_{\rm iso}$ correlation

The spectral parameter evolution is also commonly reported within one pulse in the burst[17],[49]. Thanks to the large effective area of the WAM, we can obtain the "finer"-timer-resolved spectra for a bright GRB and can investigate the spectral parameter correlation even within one pulse. Ohno et al. (2009) performed the spectral analysis for time-resolved spectra divided into 1-sec resolution for the bright GRB 061007 and found that even we see the inside of each pulse, the spectral parameter evolution, the $E_{\rm peak} - L_{\rm iso}$ relation follow the same manner as that of each pulse-resolved analysis, $E_{\rm peak} \propto L_{\rm iso}^{0.46\pm0.03}$ as shown in figure 15. Interestingly, we also found that the pulse-rising phase seems to follow the different trend from that of the pulse-decay phase. Here, we can constrain the fireball dynamics based on both the simple synchrotron shock scenario and the photospheric emission scenario. The $E_{\rm peak} - L_{\rm iso}$ relation can be written from these two scenarios as; $E_{\rm peak} \sim 3\varepsilon_B^{1/2}\varepsilon_e^{3/2}L_{\gamma,52}^{1/2}r_{13}^{-1}$ (synchrotron) and $E_{\rm peak} \sim \Gamma_e^{1/2}r_{10}^{-1/2}L_{\gamma,52}^{1/4}$ (photospheric), here ε_B and ε_e are the fraction of the total energy goes into the magnetic amplification and the electron acceleration and Γ is the bulk Lorentz factor of the fireball expansion. Looking at these formula, the differences between pulse-rising and -decay phase suggest that the evolution of the bulk Lorentz factor and/or emitting region within the pulse.

Another interesting example observed by the WAM is the ultra-long GRB 060814. Althogh the redshift of this burst could not be determined, the duration was extremely long, larger than 1000 sec and the pulse consists of only one simple FRED-like structure. Therefore, this burst is a good candidate to explore the difference between pulse-rising and -decay phase in detail. Sugita et al. (in prep) also found the pulse-decay phase follow the same relation of $E_{\rm peak} \propto F^{0.51\pm0.09}$ as shown in the figure 16 but the pulse-rising does not follow this $E_{\rm peak} \propto F^{0.5}$ relation. This could

be explained by the transition from the thermal emission to the non-thermal emission phase. The detailed discussion will be presented in the following paper.

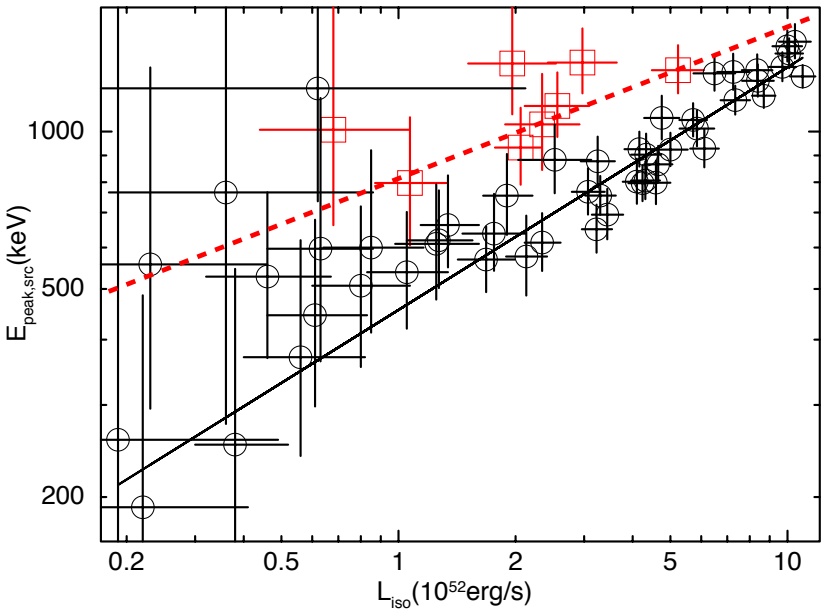

Figure 15: Correlation between E_{peak} and L_{iso} using 1-sec time-resolved spectra for the bright long GRB 061007. Black open circles and red squares show the data which belong to the pulse-decay and -rising phase, respectively. The best fit model for each population is also shown by the black-solid and red-dashed lines[40].

3.4 WAM view of solar flares

We have already published the WAM 1st solar flare catalog[43] using 105 solar flare events observed by the WAM between the period of 2005 to 2009 and investigated several spectral parameter correlations between each event such as soft X-ray flux observed by the GOES (1.55-12.4 keV)satellite and the hard X-ray flux observed by the WAM (100-300 keV), duration and flux, and duration and photon index. This study revealed that the soft X-ray flux and hard X-ray flux shows a positive correlation as shown in figure 17, suggesting the thermal bremsstrahlung emission by accelerated particles can be seen for many flares up to 100-300 keV. Ishikawa et al. (2013) confirmed this trend for the B-class microflares by performing the RHESSI/WAM detailed joint spectral analysis. On the other hand, we do not find clear correlation between the hard X-ray flux and the photon index, indicating that some large flares could be formed by the combinations of many small flares. We are now compiling the WAM second solar flare catalog including longer period data, covering both solar minimum and maximum phase (Yabe+ in prep). In this analysis, we confirmed the trend that the soft X-ray and hard X-ray flux still keep the positive correlation as we found in the 1st solar flare catalog, and also we do not find any clear correlation for the hard X-ray flux and the photon index.

3.5 WAM view of SGRs -short bursts from AXP 1E 1547.0-5408

The Anomalous X-ray Pulsar (AXPs) and the Soft Gamma Repeater (SGRs) are believed to

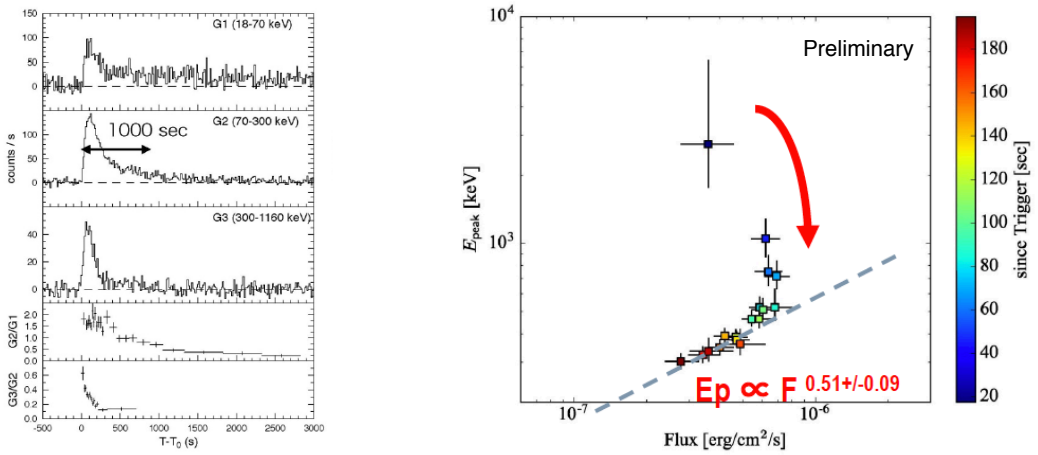

Figure 16: The light curve of the ultra-long GRB 080614B obtained by the Konus-Wind (left). The WAM also observed this GRB, but only available up to 200 s after the trigger because of the earth occultation. The $E_{\rm peak}$-Flux correlation for this burst (right). The color gradation show the time evolution as indicated in the color chart.

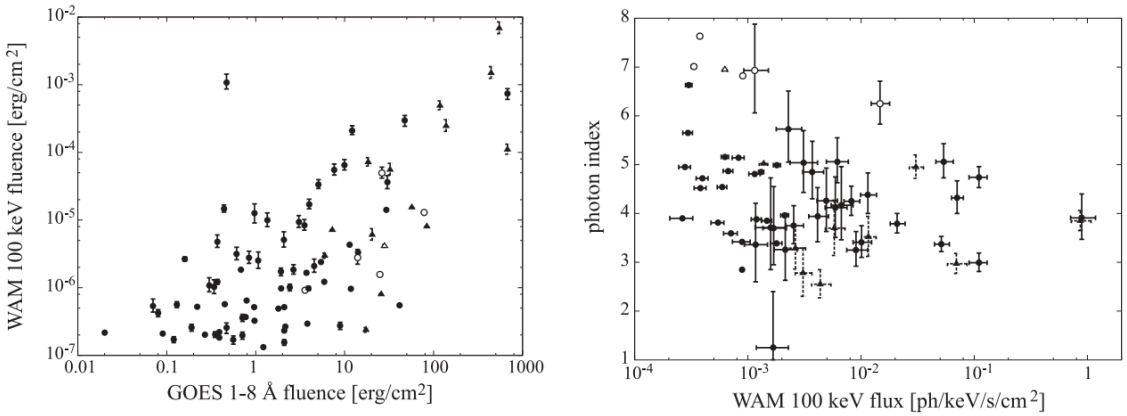

Figure 17: Spectral parameter correlations for the solar flares obsereved by the WAM between 2005 to 2009. The relation between the soft X-ray flux (1.55-12.4 keV: GOES) and the hard X-ray flux (100-300 keV: WAM) (left) and the relation between the hard X-ray flux and the photon index (right)[43]

be an extremely magnetized neutron star with $\sim 10^14$ G, "magnetar"[25][27][31]. Although, the hard X-ray emission for those objects is relatively soft for the WAM energy band in the quiescence state, the WAM successfully detected the hard X-ray emission from at least three such objects: SGR 1806-20, SGR 1900+14 and SGR J1550-5418. As for the SGR J1550-5418 (AXP 1E 1547.0-5408) showed anomalous bursting phase within only one day (January 22, 2019) and the WAM detected at least 568 short bursts whose duration is less than 1 s as shown in figure 18 left[41]. These bursts have been also reported by many other detectors[38][33][37][35][32]. Yasuda et al. (2015) and Yasuda (2016) analyzed 78 bursts and found that the most of WAM spectra (58 out of 78) can be fit by the single black body spectrum with a temperature of around 14 keV and some of spectra required extra component with power-law (11 spectra) and cutoff power-law (8 spectra). Figure 18 right shows example of the spectrum which need an extra component. Thanks to the large effective area of the WAM, we have detected MeV photons from magnetar flare. The black body emission with kT=14 keV can be expected by the trapped electron/position photon plasma with magnetic field of B$>10^{13}$ G[13]. It is interesting to investigate the origin of the extra component. One possibility is the 511 keV annihilation line and another exotic scenario is the photon splitting in the strong magnetic field.

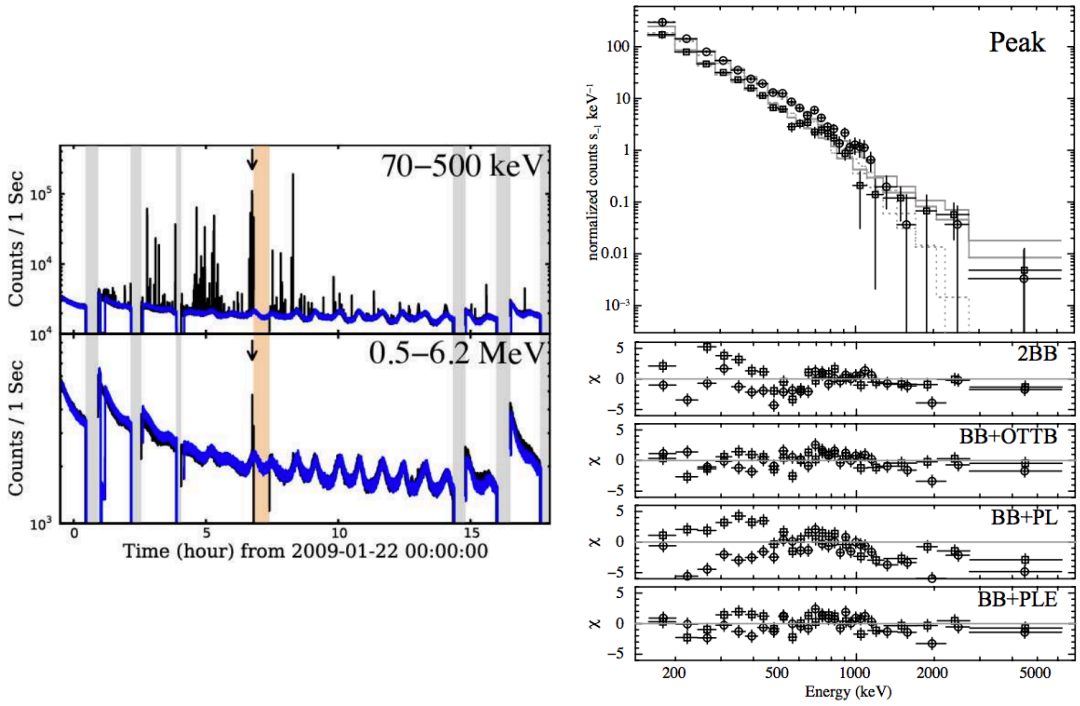

Figure 18: Left: Light curves of the AXP 1E 1547.0-5408 obtained by the WAM-0 detector in two energy bands: 70-500 keV (top) and 0.5-6.2 MeV (bottom). Right: Example of spectrum of the hardest short obtained by the WAM-0 (circle) and the WAM-1 (square), respectively. Bottom part of this figure show the residuals from the various spectral modeling: two black body models, black body plus optically-thin thermal bremsstrahlung (OTTB), black body plus power-law and black body plus power-law with exponential cutoff, respectively.

3.6 Monitoring of bright gamma-ray sources

The all-sky monitoring of hard X-ray and soft gamma-ray sources is very important for investigating of the origin of the variability. The Crab nebula is one of the brightest X-ray source in the sky and the observed flux of the Crab nebula is almost stable to be used as the standard calibration source, however, recent monitoring observations of the Crab revealed the flux variability around 10% from 10-500 keV by multiple instruments[47][54][19]. Another interesting source is the black hole binaries such as Cyg X-1. Such objects sometimes exhibit a transition for its flux and spectral shape, so called a state transition and it is believed that the origin of such transitions is the change of the physical condition of the disk/corona around the black hole and a possible jet contribution[39][45][48]. A continuous monitoring up to gamma-ray energy band is important to investigate the physical origin of such variability. Although the WAM is not designed to perform such continuous monitoring, the sudden flux variation due to the ingress/egress of the objects behind the earth enable us the continuous flux monitoring for such bright gamma-ray sources. This earth occultation technique has been widely utilized for all-sky monitoring for such steady sources by CGRO-BATSE[7] and Fermi-GBM[47][50]. We also apply this techinique to the WAM data and successfuly detected several bright gamma-ray objects: Crab, CygX-1, GX339-4, and CentaurusA. Figure 19 left shows the 6-years integrated spectrum of the Crab nebula together with hard X-ray spectrum obtained by the Suzaku-HXD. The WAM detected photons from the Crab nebula up to 600 keV and the spectral shape is almost consistent with that of hard X-ray band. A hint for an additional spectral break around 200 keV can be seen but it was not statistically significant. We also extracted the 6-years monitoring light curve of the Cyg X-1 as shown in figure 19 right and successfully detect the state transition from high/soft to low/hard state by the WAM data up to soft gamma-ray energy band. The spectrum does not require the extra hard component in the hard state reported by the INTEGRAL-IBIS probably due to the thermal Comptonization component is still dominant up to 600 keV, and more sensitive observation above 500 keV is important to investigate such component.

4. Conclusions

The Suzaku Wide-band All-sky Monitor (Suzaku-WAM), which consists of 20 large/thick BGO crystals surrounding the main detector of the Suzaku-HXD, is a very powerful all-sky monitor in the hard X-ray and soft gamma-ray energy band. During 10 years operation from 2005 to 2015, all of the 20 detectors are operated without problems and successfully detected more than 1400 GRBs. The GRB detection rate is about 140 GRBs per year, which is comparable to other GRB-specific missions. The energy response of the WAM is calibrated by both ground and in-orbit calibrations and the uncertainty is found to be 10-30%. Thanks to its large effective area of ~ 600 cm^2 even at 1 MeV and the joint analysis with the Swift/BAT enable us to perform the analysis for the spectral parameter distribution and its correlations, removing an observational bias effect as much as possible, and revealed that the finer time-resolved analysis is a very powerful tool to investigate the emission mechanism of GRBs and the physical condition of the expanding fireball.

More than 1000 solar flares and SGR bursts have been detected by the WAM. The large effective area of the WAM can detect the hard X-ray emission from both bright solar flares and

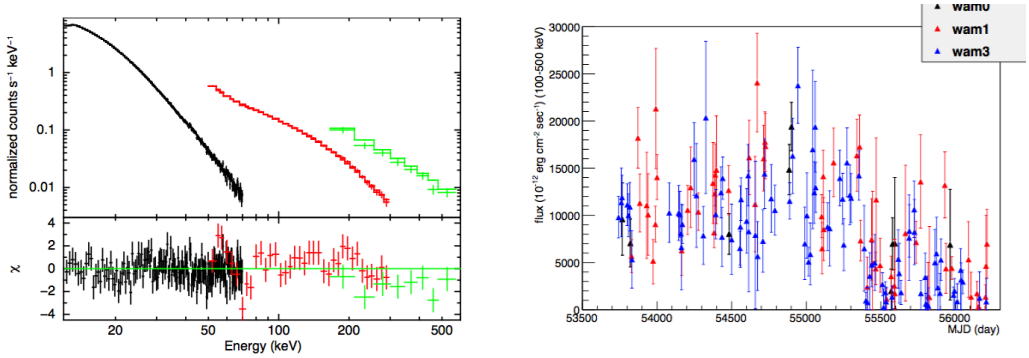

Figure 19: The 6-years integrated Crab spectrum (left) obtained by the WAM-0 detector (green: 200-600 keV band) compared with that of obtained by the HXD-PIN (black) and HXD-GSO(red). This broad-band spetrum is fit by the broken power-law with a fixed photon index of 2.09 and 2.27 and a break energy of 103 keV, which are reported by Kokubun et al. (2007) and Yamada et al. (2011). The fit looks reasonable, but systematic residuals in the WAM energy band can be seen. However, additional break does not improve the fit significantly. The long term light curve of Cyg X-1 (right) obtained by the WAM-0 (black), WAM-1 (red), and WAM-2 (blue) detectors, respectively. All the detectors show a consistent trend and the state transition from the high/soft to the low/hard can be seen around MJD=55500.

microflares and systematic analysis for any types of solar flares could be useful to investigate the particle acceleration conditions in the solar flares. The MeV emission from SGR has been detected by the WAM and it could be very interesting to discuss the fundamental physics in the extreme physical condition (e.g., large magnetic field). As we described throughout this paper, the wide-band and high-sensitive GRB observations still have to keep an another important direction for the future monitoring observations for the hard X-ray and soft gamma-ray sky, in addition to a quick and precise localization, which will be required for the follow-up observations of the gravitational wave sources. The WAM type of all-sky instrument is expected to be equipped in the Japanese future proposing missions: Wideband Hybrid X-ray Image (WHXI) onboard Focusing On Relativistic universe and Cosmic Evolution (FORCE)[58] and Soft Gamma-ray SpectroPolarimeter (SGSP) onboard Physics of Energetic and Non-thermal plasmas in the X region (PhoENiX).

References

[1] Colgate, S. A. 1974, ApJ, 187, 333

[2] Mazets, E. P., Golentskii, S. V., Ilinskii, V. N., Aptekar, R. L., & Guryan, Iu. A. 1979, Nature, 282, 587

[3] Golenetskii, S. V., Mazets, E. P., Aptekar, R. L., & IIyinskii, V. N, 1983, Nature, 306, 451

[4] Fishman, G. J., Meegan, C. A., Parnell, T. A.,Wilson, R. B., Paciesas, W.,Mateson, J. L., Cline, T. L.,& Teegarden, B. J. 1985, ICRC, 3, 343

[5] Paczyński, B. 1986, ApJ, 308, L43

[6] Eichler, D, Livio, M., Piran, T., & Schramm, D. N. 1989, Nature, 340, 126

[7] Harmon, B. A., Finger, M. H., Rubin, B., et al. 1992, NASA Conference Publication, 3137, 69

[8] Mészáros, P., & Rees, M. J. 1992, MNRAS, 257, 29p

[9] Rees, M. J., & Mészáros, P. 1992, MNRAS, 258, 41P

[10] Band, D., Matteson, J., Ford, L., et al. 1993, ApJ, 413, 281

[11] Woosley, S. E. 1993, BAAS, 25, 894

[12] Rees, M. J., & Mészáros, P. 1994, ApJ, 430, L93

[13] Thompson, C., & Duncan, R. C. 1995, MNRAS, 275, 255

[14] Kobayashi, S., Piran, T., & Sari, R. 1997, ApJ, 490, 92

[15] Paciesas, William S., Meegan, Charles A., Pendleton, Geoffrey N., et al. 1999, ApJS, 122, 465

[16] Fryer, C. L., Woosley, S. E., & Heger, A. 2001, ApJ, 550, 372

[17] Ryde, F., Petrosian, V., 2002 ApJ, 578, 290

[18] Zhang, B., & Mészáros, P. 2002, ApJ, 581, 1236

[19] Ling, J. C., & Wheaton, W. A. 2003, ApJ, 598, 334

[20] Ryde, F. 2004, ApJ, 614, 827

[21] Ohno M., et al. 2005, IEEE Trans. Nucl. Sci., vol. 52, no. 6, pp.2758-2764 2005

[22] Amati, L. 2006, MNRAS, 372, 233

[23] Woosley, S. E., & Bloom, J. S. 2006, ARA&A, 44, 507

[24] Yamaoka, K., Sugita, S., Ohno, M., et al. 2006, Proceedings of the SPIE, Volume 6266, id. 626643

[25] Woods, P. M., & Thompson, C. 2006, in Compact Stellar X-ray Sources, ed. W. Lewin & M. van der Klis (Cambridge, UK: Cambridge University Press), 547

[26] Cabrera, J. I., Firmani, C., Avila-Reese, V., Ghirlanda, G., Ghisellini, G., & Nava, L. 2007, MNRAS, 382, 342

[27] Kaspi, V. M. 2007, Ap&SS, 308, 1

[28] Nakar, E. 2007, Phys. Rep., 442, 166

[29] Mitsuda, K., Bautz, M., Inoue, H., et al. 2007, PASJ, 59, S1

[30] Kokubun, M., Makishima, K., Takahashi T., et al. 2007, PASJ, 59, S53

[31] Mereghetti, S. 2008, A&A Rev., 15, 225

[32] Bellm, E., Smith, D. M., & Hurley, K. 2009, GCN Circ., 8857

[33] Connaughton, V., & Briggs, M. 2009, GCN Circ. 8835

[34] Krimm, H. A., Yamaoka, K., Sugita, S. et al. 2009, ApJ, 704, 1405

[35] Golenetskii, S., Aptekar, R., Mazets, E., Pal'Shin, V., Frederiks, D., Oleynik, P., Ulanov, M., & Cline, T. 2009, GCN Circ., 8858

[36] Ryde, F., & Pe'er, A. 2009, ApJ, 702, 1211

[37] Savchenko, V., Beckmann, V., Neronov, A., Mereghetti, S., von Kienlin, A., Beck, M., Borkowski, J., & Gotz, D. 2009, GCN Circ., 8837, 1

[38] Gronwall, C., Holland, S. T., Markwardt, C. B., Palmer, D. M., Stamatikos, M., & Vetere, L. 2009, GCN Circ., 8833

[39] Motta, S., Belloni, T., & Homan, J. 2009, MNRAS, 400, 1603

[40] Ohno, M., Ioka, K., Yamaoka, K., et al. 2009, PASJ, 61 201

[41] Terada, Y, et al. 2009, GCN Circ., 8845

[42] Yamaoka, K., et al. 2009, PASJ, 61, S35

[43] Endo, A., Minoshima, T., Morigami, K., et al. 2010, PASJ, 62, 1341

[44] Sugita, S. 2010, PhD thesis, Aoyama Gakuin University

[45] Laurent, P., Rodriguez, J., Wilms, J., et al. 2011, Science, 332, 438

[46] Sakamoto, T., et al. 2011, PASJ, 63, 215

[47] Wilson-Hodge, C. A., Cherry, M. L., Case, G. L., et al. 2011, ApJL, 727, LL40

[48] Jourdain, E., Roques, J. P., Chauvin, M., & Clark, D. J. 2012, ApJ, 761, 27

[49] Lu, R., Wei, J., Liang, E., et al. 2012, ApJ, 756, 112

[50] Wilson-Hodge, C. A., Case, G. L., Cherry, M. L., et al. 2012, ApJS, 201, 33

[51] Vilmer, N., 2012, Philosophical Transactions of the Royal Society A: Mathematical, Physical and Engineering Sciences, vol. 370, issue 1970, pp. 3241-3268

[52] Ishikawa, S., Krucker, S., Ohno, M., Lin, Robert P., 2013, ApJ, 765, 143

[53] Yamada, S., Negoro, H., Torii, S., et al. 2013, ApJL, 767, LL34

[54] Kouzu, T., Tashiro, M. S., Terada, Y., et al. 2013, PASJ, 65, 74

[55] Connaughton, V., Briggs, M. S., Goldstein, A., et al. 2015, ApJS, 216, 32

[56] Fujinuma, T., 2015, Master thesis, Saitama University, Japan

[57] Ohmori, N., Yamaoka, K., Ohno, M., et al. 2016, PASJ, 68, 30

[58] Mori, K., Tsru, T. G., Nakazawa, K., et al. 2016, Proceedings of the SPIE, 9905E, 1OM

[59] Yamaoka, K., Ohno, M., Tashiro, M., et al. 2017, PASJ, 69, 21